Mathematics and Computers in Simulation 229 (2025) 1–14

Contents lists available at ScienceDirect

Mathematics and Computers in Simulation

journal homepage: www.elsevier.com/locate/matcom

Original articles

Analysis of non-uniform grid-forming control techniques for the HVDC connection of renewable energy

Adrián Beneit-Barajas *, Patricia Penades-Huesca, Jaime Martínez-Turégano

Research Institute on Automatics and Industrial Informatics (ai2), Universitat Politècnica de València, Valencia, Spain

ARTICLE INFO

Keywords:
Grid-forming
Droop
Virtual synchronous machine
Offshore wind power plants
Diode-rectifier

ABSTRACT

Grid-forming control techniques are required to achieve a high penetration of power electronics-based renewable energy sources for decarbonized electric systems. However, different grid-forming control strategies can operate in the same grid, and grid stability shall be warranted. This paper analyses the use of different grid-forming control strategies for diode rectifier-based wind power plants. The analysed grid-forming controllers are the well-known droop control, an advanced droop control, and the virtual synchronous machine control. The controllers' analysis validates the three grid-forming controllers' interoperability, identifying each control parameter's contribution to the stability of each system state variable. Furthermore, the analysis allows a better tuning of the control parameters. Additionally, a fault-ride-through strategy that improves the system restoration after faults is proposed and validated. The proposed fault-ride-through strategy achieves a soft restoration of the active power.

1. Introduction

The challenges produced by climate change, along with the increasing concerns about energy supply and costs, are gaining relevance among government authorities and society. Consequently, national administrations reevaluate their energy generation strategies by increasing their renewable resources. Offshore wind power plants (WPPs) are expected to provide global energy due to high wind speeds and stable conditions.

Different alternatives have been explored to integrate offshore WPPs generation into the grid through high-voltage direct current (HVDC) grids, as [1], which compares some control methods for Multi-Terminal HVDC systems. Diode rectifiers (DRs) are a technical solution for linking offshore WPPs to an HVDC grid. This approach, employed within the study, reduces the cost of offshore WPPs by up to 30% while also improving the efficiency and reliability of the entire system [2–4]. Recent investigations such as [5,6] propose novel control solutions for the offshore WTGs connected through DRs but the coexistence of different grid-forming controllers among the WPP is not addressed.

Installed WPPs are integrated into the electrical grid with grid-connected converters operating in grid-following mode. WTGs require a connection to the electrical grid to operate without an inertia control loop, which makes them incapable of responding to dynamic frequency changes in the system. Conversely, grid-forming WTGs can establish their own grid without an external grid. This technology benefits grid restoration after an outage, demonstrating their self-sufficiency and resilience in power generation and grid support [7,8].

Different grid-forming controls (droop, Virtual Synchronous Machine, dispatchable Virtual Oscillator Control) are compared to find a generic grid-forming model in [9]. Yet, they were individually tested when connected to the infinite power grid through an LCL filter instead of a converter-dominated grid, and their interoperability was not tested.

* Corresponding author.
E-mail address: adbeba@upv.edu.es (A. Beneit-Barajas).

https://doi.org/10.1016/j.matcom.2024.09.014
Received 19 January 2024; Received in revised form 3 July 2024; Accepted 16 September 2024
Available online 20 September 2024

In [10], authors compare three types of grid-forming controls (droop, synchronverter, and matching control). They evaluate the performance of these controls in a system-level simulation case study that uses the IEEE 9-bus test system. The study examines their performance in black start, set-point tracking, and load-sharing. However, the system has three identically tuned grid-forming controllers in the main system, so the interoperability between them is not studied nor tested in a DR-based WPP. In [11], researchers conducted additional studies to analyse the black start process using four grid-forming controls: Direct Power Control, VSM, Power Synchronous Control, and Distributed-PLL based. The study involved a system in which 400 MW WPPs were connected to an onshore AC grid. Nevertheless, the study addresses neither the interoperability of different grid-forming control strategies nor fault-ride through.

Some recent investigations analyse the dynamic relationship between grid-forming converters operating in parallel in the same grid. [12] studies the operation of several aggregated VSMs, finding design procedures to ensure stability by decoupling outer and inner control loops when the number of parallel converters increases. However, the aggregated converters had identical control strategies.

Special attention to researches [13,14] that employ eigenvalue analyses to study the system stability when two identical grid-forming controllers feed a common load, concluding that even controllers with identical dynamics can oscillate against each other. They respectively found that proper selection of the filter inductance and voltage feed-forward into the current controller can prevent instabilities. Still, a grid-forming controller was tested without any control parameter optimization to ensure stability, avoiding filter inductance selection. A specific case is investigated in [15] where it was proved that capacitive loads lead to instability if the controllers reach current saturation. However, there is still a need to explore the interaction between grid-forming converters with different control strategies.

On the other hand, grid-forming and grid-following WTGs interoperability was tested when connected to a DR-based HVDC link using the same fault-ride-through strategy [16]. Therefore, no considerations have been made regarding the interoperability between different grid-forming controllers in offshore WPPs connected to DR-HVDC.

However, most research focuses on the grid-forming control during steady-state conditions without considering the fault-ride-through capability. In [17], the authors propose a grid-forming controller with two active power loops to maintain the frequency and the AC offshore voltage. The proposed control includes a current control loop for current limitations during faults without any strategy to achieve a soft restoration after faults.

In [18], the fault ride-through capability of a 40 MW offshore wind farm remained examined using the EOn grid code. Nevertheless, alternative control methodologies and their combination between controls were not investigated. Moreover, [19] uses only droop control and proposes a fault-mode controller and dynamic virtual damping controller to test during very weak-grid conditions. [20] considered three different control schemes (Virtual Synchronous Machine, Distributed PLL-based, and Power Synchronization Control). These control schemes are implemented in an islanded grid where WTGs supply power to a passive load, evaluating their performance during three-phase symmetrical faults. As seen in this paper, the compatibility among different types of grid-forming control during faults has not been thoroughly studied or only studies one controller.

[21] includes an improved current limiting control method for a grid-forming system with an adaptive virtual impedance. This impedance automatically adjusts, adapting to various fault situations in the power grid. Furthermore, [22] proposes a method to adapt the droop gain with respect to the current magnitude, improving the stability limit and dynamic behaviour, but for advanced droop and VSM is not proved.

Therefore, the main objective of this paper is to analyse the effects that WPP converters with different grid forming strategies would have on the overall system small signal stability and also on fault recovery, considering the specific case where the WPP is connected to an HVDC link via a diode rectifier. To that avail, this paper conducts an analytical study to test the technical feasibility and interoperability of the HVDC connection for a mix of grid-forming sources. The study includes a small signal stability analysis with three grid-forming controllers (droop control, advanced droop control and VSM) that allow a proper tuning of the grid-forming controller parameters, ensuring stability and maximizing performance. Results with active power reference changes are included to validate the interoperability of the three considered grid-forming controllers. The paper also includes a fault-ride-through strategy that achieves a soft power restoration. Then, simulation results with faults are included to validate the fault strategy. The presented procedure allows for detailed small signal and fault analysis of mixed grid-forming techniques, showing that adequate tuning of all WPP grid-forming parameters is required for robust, stable operation of the complete system.

This paper consists of five sections and includes a description of the system, the three grid-forming control strategies, a small signal stability analysis to study the interoperability of the controllers, including the proposed fault-ride-through strategy, simulation results that validate the compatibility of the controller and the fault strategy, and a discussion of the corresponding conclusions.

2. System description

2.1. General system description

The proposed system consists of an offshore WPP connected to an onshore grid via a DR-HVDC link, as depicted in Fig. 1. The WPP comprises 3 clusters with 50 Type-4 grid-forming WTGs, with a total nominal power of 400 MW each. These WTGs are aggregated following the technique proposed in [23]. Furthermore, the DR-HVDC link includes three DR platforms connected in series on the DC side and in parallel on the AC side. Each DR station contains two 12-pulse DR bridges, complemented by the respective transformers and AC filters.

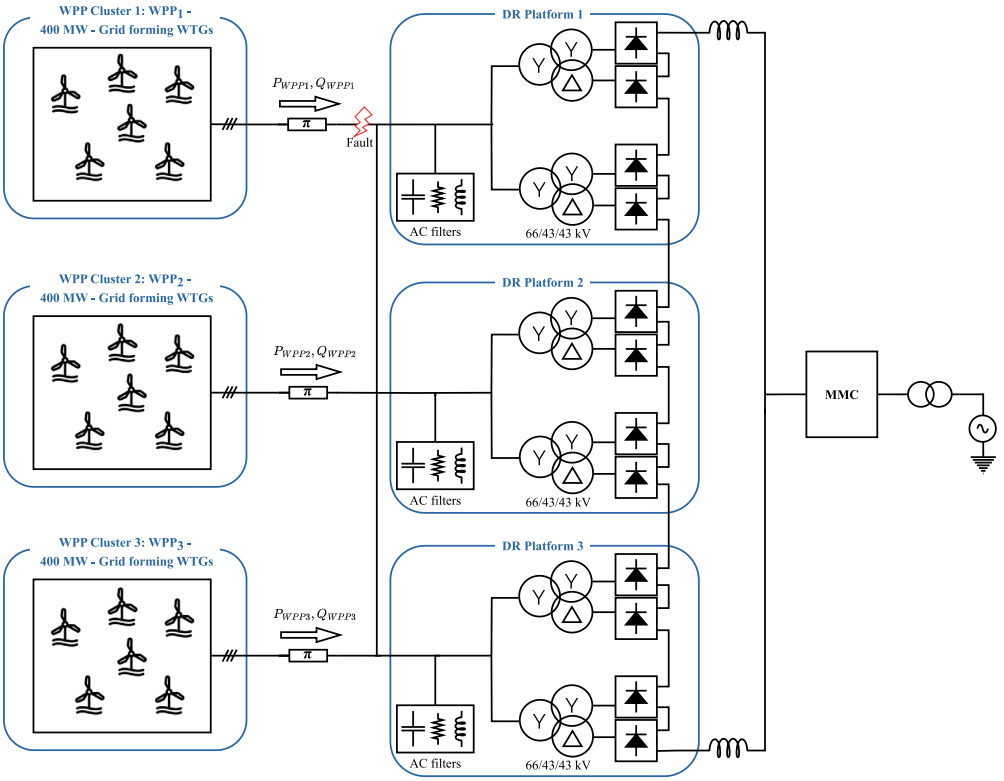

Fig. 1. WPP with 3 clusters of 400 MW, each one connected to the on-shore grid through a DR-based HVDC link.

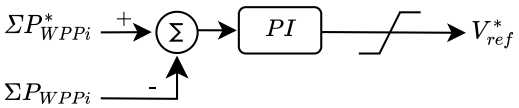

Fig. 2. Wind power plant controller.

2.2. Control strategy

The strategy implemented for controlling the offshore WPP consists of a Wind Power Plant controller that regulates the power transmission through the DR-HVDC link and the WTG controls, which include voltage and current loops and the power-sharing controllers. Fig. 2 shows the Wind Power Plant controller, which sets the reference voltage magnitude (V^*_{ref}) for all WTGs. The control consists of a PI controller that uses the sum of the produced active power (P_{WPPi}) and the available WTG power (P^*_{WPPi}). Eq. (1) shows this control strategy, where $\sum P^*_{WPPi} = P^*_{WPP1} + P^*_{WPP2} + P^*_{WPP3}$ and $\sum P_{WPPi} = P_{WPP1} + P_{WPP2} + P_{WPP3}$. The Wind Power Plant Controller is implemented with a 10 ms sampling period (400 times slower than the WTG controllers), with an additional 10 ms delay.

$$V^*_{ref}(s) = \left(\sum P^*_{WPPi} - \sum P_{WPPi}(s)\right)\left(K_{p,Vref} + \frac{K_{i,Vref}}{s}\right) \tag{1}$$

Fig. 3 shows the grid side converter control of each WTG. It is divided into two levels: the power-sharing control and a cascaded control loop that regulates voltage and current. Each WTG has a fault ride-through strategy to restore the system after faults. This approach ensures efficient and stable energy generation by enabling effective coordination throughout the offshore WPP, with each control level playing a specific role in optimal system performance.

2.2.1. Wind turbine grid-forming power control

Each WTG implements a P/ω and Q/V grid-forming controller that sets the phase and magnitude of the reference voltage for each WTG. The controller uses filtered active power ($\widehat{P}_{WPPi}$) to calculate the angular frequency (ω), which is then used to calculate the voltage angle of the WTGs grid-side converters. In parallel, the filtered reactive power ($\widehat{Q}_{WPPi}$) is used to calculate the voltage magnitude ($V_{i,d}$) of each WTG. Local measurements of active power (P_{WPPi}) and reactive power (Q_{WPPi}) are filtered with a 10 rad/s low pass filter. Three different grid-forming controllers are designed and compared:

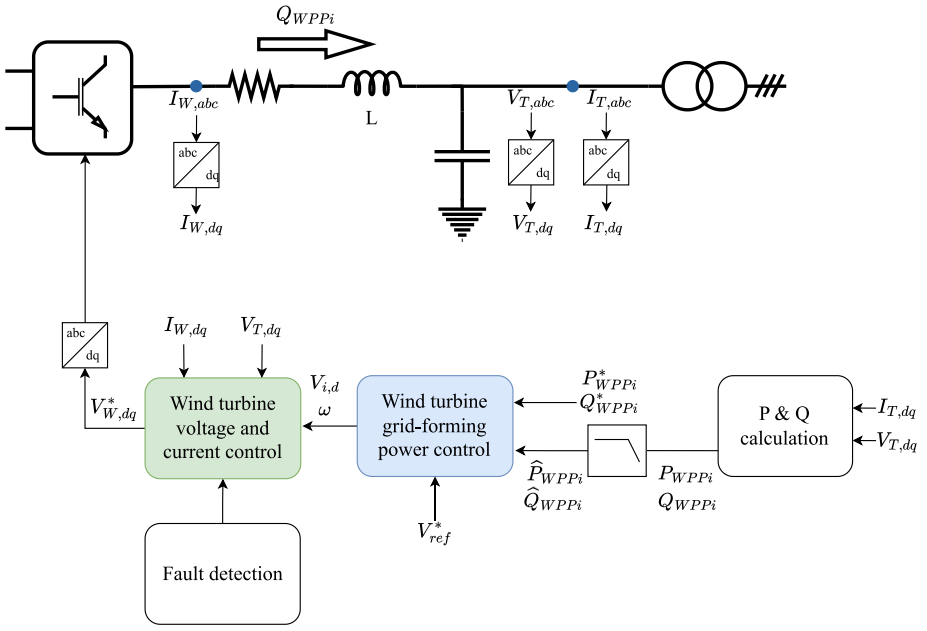

Fig. 3. Control strategies for grid-forming WPPs.

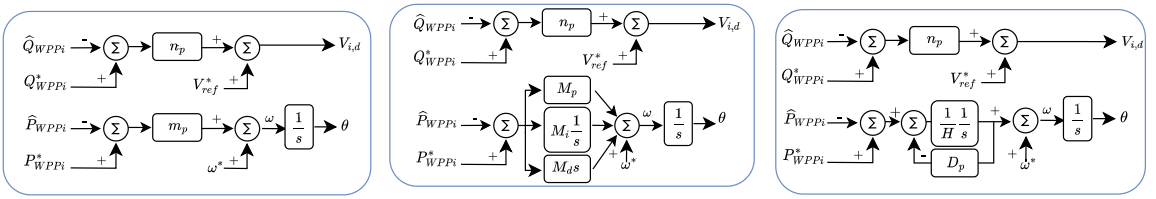

(a) Droop control (b) Advanced droop control (c) Virtual Synchronous Machine (VSM)

Fig. 4. Grid-forming control strategies.

- Droop control: calculates the angular frequency (ω) and the voltage ($V_{i,d}$) for WTGs' grid-side converters based on the active power and reactive power values [24,25]. A proportional droop gain (m_p) is used for this, as shown in Fig. 4(a). Eq. (2) describes the angular frequency (ω) calculation, and Eqs. (3) and (4) describe how the dq voltage reference ($V_{i,dq}$) is calculated.

$$\omega = \omega^* + m_p(P^*_{WPPi} - \widehat{P}_{WPPi}) \tag{2}$$

$$V_{i,d} = V^*_{ref} + n_p(Q^*_{WPPi} - \widehat{Q}_{WPPi}) \tag{3}$$

$$V_{i,q} = 0 \tag{4}$$

- Advanced Droop Control: is an improved version of droop-based control. This control method introduces two additional coefficients for active power control: the derivative coefficient (M_d) and the integral coefficient (M_i). By using this approach (shown in Fig. 4(b)), transient response characteristics can be modified while still maintaining the static droop behaviour [26]. The frequency is generated using Eq. (5), while Eqs. (3) and (4) remain unchanged in this control.

$$\omega = \omega^* + \left(M_p + \frac{M_i}{s} + M_d s\right)(P^*_{WPPi} - \widehat{P}_{WPPi}) \tag{5}$$

- Virtual Synchronous Machine (VSM): it replicates the dynamic properties of a conventional synchronous generator using a power converter. This method is useful in renewable energy and distributed generation systems as it integrates the benefits of synchronous generators, such as inertia and islanded operation. VSM provides the flexibility to fine-tune its parameters to suit the specific requirements of the grid or installation. The generator mechanical swing equation is emulated with inertia constant (H) and damping gain (D_p). The frequency and active power relation are the same as for droop control (Fig. 4(c)). Eq. (6) generates the frequency, and Eqs. (3) and (4) remain unaltered.

$$\omega = \omega^* + \left(\frac{1}{Hs + D_p}\right)(P^*_{WPPi} - \widehat{P}_{WPPi}) \tag{6}$$

2.2.2. Wind turbine voltage and current control

Eqs. (7) and (8) describe the voltage control loop, while Eqs. (9) and (10) describe the current control loop. $V_{i,d}$ is the reference voltage generated by grid-forming control through Eqs. (3). $K_{p,Vd}$, $K_{i,Vd}$, $K_{p,Id}$ and $K_{i,Iq}$ are the proportional and integral of the PI controllers, and $V_{T,d}$, $V_{T,q}$, $I_{T,d}$ and $I_{T,q}$ represent the measured voltage and current in d and q axis (Fig. 3).

$$I_d^* = (V_{i,d} - V_{T,d})\left(K_{p,Vd} + \frac{K_{i,Vd}}{s}\right) + I_{T,d} \tag{7}$$

$$I_q^* = (V_{i,q} - V_{T,q})\left(K_{p,Vq} + \frac{K_{i,Vq}}{s}\right) + I_{T,q} \tag{8}$$

$$V_{W,d}^* = (I_d^* - I_{W,d})\left(K_{p,Id} + \frac{K_{i,Id}}{s}\right) + (V_{T,d} - I_{W,q}L\omega^*) \tag{9}$$

$$V_{W,q}^* = (I_q^* - I_{W,q})\left(K_{p,Iq} + \frac{K_{i,Iq}}{s}\right) + (V_{T,q} + I_{W,d}L\omega^*) \tag{10}$$

2.3. Problem statement

Different grid-forming controllers have been tested in previous research efforts. However, the novelty of this study lies in evaluating their interoperability. In particular, this study involves applying different control strategies in each WPP cluster and analysing its stability. Moreover, each WTG implements a fault ride-through strategy that allows system recovery after clearing faults and achieves a soft restoration to normal operation. The proposed fault ride-through strategy modifies the parameters of the grid-forming control when a fault occurs. Once the fault is cleared and the system is restored, these values revert to their original state.

3. Controller implementation

3.1. Design methodology

The offshore grid is represented by its most impactful components, including each WPP's coupling transformer and a common capacitor that characterizes the interconnection lines and the DR filters. A transformer linked to the rectification process's equivalent point represents the DR system. All component values are referred to the WPP voltage level and can be found in Table 3. Eqs. (11)–(16) rule the described circuit and are defined in a dq reference frame rotating at nominal frequency.

$$V_{WPP,i,d} = i_{WPP,i,d}R_{WPP} + \frac{di_{WPP,i,d}}{dt}L_{WPP} - \omega^* L_{WPP} i_{WPP,i,q} + V_{C,d} \tag{11}$$

$$V_{WPP,i,q} = i_{WPP,i,q}R_{WPP} + \frac{di_{WPP,i,q}}{dt}L_{WPP} + \omega^* L_{WPP} i_{WPP,i,d} + V_{C,q} \tag{12}$$

$$V_{C,d} = i_{DR,d}R_{DRT} + \frac{di_{DR,d}}{dt}L_{DRT} - \omega^* L_{DRT} i_{DR,q} + V_{DR,d} \tag{13}$$

$$V_{C,q} = i_{DR,q}R_{DRT} + \frac{di_{DR,q}}{dt}L_{DRT} + \omega^* L_{DRT} i_{DR,d} + V_{DR,q} \tag{14}$$

$$i_{C,d} = C\frac{dV_{C,d}}{dt} - \omega^* C V_{C,q} \tag{15}$$

$$i_{C,q} = C\frac{dV_{C,q}}{dt} + \omega^* C V_{C,d} \tag{16}$$

$$\sum i_{WPP,i,dq} = i_{C,dq} + i_{DR,dq} \tag{17}$$

Eqs. (18) and (19) describe each WPP's filtered active and reactive power ($\hat{P}_{WPP,i}$, $\hat{Q}_{WPP,i}$).

$$\frac{d\hat{P}_{WPP,i}}{dt} = \omega_f\left(\frac{3}{2}(V_{WPP,i,d}i_{WPP,i,d} + V_{WPP,i,q}i_{WPP,i,q}) - \hat{P}_{WPP,i}\right) \tag{18}$$

$$\frac{d\hat{Q}_{WPP,i}}{dt} = \omega_f\left(\frac{3}{2}(V_{WPP,i,q}i_{WPP,i,d} - V_{WPP,i,d}i_{WPP,i,q}) - \hat{Q}_{WPP,i}\right) \tag{19}$$

Finally, the remaining equations refer to the control algorithms defined in Section 2. The cascaded voltage and current control are omitted from the system's equations, assuming they are properly tuned to generate the targeted voltage waveform at the WPP's output. Consequently, the focus can be directed towards the power-sharing controllers.

Each WPP cluster integrates one of the three grid-forming control strategies listed in Section 2.2.1. Eqs. (20)–(25) describe the system dynamics to apply the control strategies of Eqs. (2), (5), and (6). The γ variables are added to account for the dynamic control laws of advanced-droop and VSM control algorithms. The N coefficient corresponds to the fast filter required to make the PID transfer function proper.

$$\frac{d\delta_1}{dt} = m_p(P_{WPP,1}^* - \hat{P}_{WPP,1})\frac{\omega^*}{P_{nom}} \tag{20}$$

Table 1
Maximum variation of eigenvalue position for the 30 considered cases.

Maximum variation of eigenvalue position for the 30 considered cases						
$\lambda_5 = 0.2845$;	$\lambda_{15,16} = 0.2824$;	$\lambda_{17,18} = 0.2345$;	$\lambda_{13,14} = 0.1317$;	$\lambda_{12} = 0.1003$;	$\lambda_{10,11} = 0.0182$;	$\lambda_{6,7} = 0.0167$;
$\lambda_{21} = 0.0080$;	$\lambda_{20} = 0.0078$;	$\lambda_{8,9} = 0.0014$;	$\lambda_{19} = 0.0003$;	$\lambda_{3,4} = 0.0003$;	$\lambda_{1,2} = 0.0002$;	$\lambda_{22} = 0.0000$

$$\frac{d\delta_2}{dt} = (M_p(P^*_{WPP,2} - \hat{P}_{WPP,2}) + M_i\gamma_1 + M_iN\gamma_2 - N^2M_d\gamma_1 - M_dN(P^*_{WPP,2} - \hat{P}_{WPP,2}))\frac{\omega^*}{P_{nom}} \tag{21}$$

$$\frac{d\delta_3}{dt} = \gamma_3 \tag{22}$$

$$\frac{d\gamma_1}{dt} = (P^*_{WPP,2} - \hat{P}_{WPP,2}) - N\gamma_1 \tag{23}$$

$$\frac{d\gamma_2}{dt} = \gamma_1 \tag{24}$$

$$\frac{d\gamma_3}{dt} = (P^*_{WPP,3} - \hat{P}_{WPP,3})\frac{\omega^*}{P_{nom}H} + \frac{D_p\gamma_3}{H} \tag{25}$$

Eqs. (2)–(6) denote the produced dq voltage references ($V_{i,dq}$) generated by the control strategies. However, these voltages are defined within the local WPP's reference frame. The variable δ_i, such that $\dot{\delta}_i = \omega_i - \omega^*$, is introduced to correlate them to the common reference frame employed in Eqs. (11)–(19).

$$\begin{pmatrix} V_{i,d,local} \\ V_{i,q,local} \end{pmatrix} = \begin{pmatrix} \cos(\delta_i) & \sin(\delta_i) \\ \sin(\delta_i) & \cos(\delta_i) \end{pmatrix} \cdot \begin{pmatrix} V_{i,d,common} \\ V_{i,q,common} \end{pmatrix} \tag{26}$$

Substituting expressions (3) and (4) into (11)–(19) and replacing the variables in local axis through (26) yields (27)–(34) as follows:

$$\frac{di_{WPP,i,d}}{dt} = ((V^*_{ref} + n_p(Q^*_{WPP,i} - \hat{Q}_{WPP,i})\frac{V_{nom}}{P_{nom}})\cos(\delta_i) - i_{WPP,i,d}R_{WPP} + i_{WPP,i,q}L_{WPP}\omega^* - V_{C,d})\frac{1}{L_{WPP}} \tag{27}$$

$$\frac{di_{WPP,i,q}}{dt} = ((V^*_{ref} + n_p(Q^*_{WPP,i} - \hat{Q}_{WPP,i})\frac{V_{nom}}{P_{nom}})\sin(\delta_i) - i_{WPP,i,q}R_{WPP} - i_{WPP,i,d}L_{WPP}\omega^* - V_{C,q})\frac{1}{L_{WPP}} \tag{28}$$

$$\frac{di_{DR,d}}{dt} = (V_{C,d} - i_{DR,d}R_{DRT} + \omega^*L_{DRT}i_{DR,q} - V_{DR}\cos(\delta_{DR}))\frac{1}{L_{DRT}} \tag{29}$$

$$\frac{di_{DR,q}}{dt} = (V_{C,q} - i_{DR,q}R_{DRT} - \omega^*L_{DRT}i_{DR,d} - V_{DR}\sin(\delta_{DR}))\frac{1}{L_{DRT}} \tag{30}$$

$$\frac{dV_{C,d}}{dt} = (\sum i_{WPP,i,d} - i_{DR,d} + \omega^*CV_{C,q})\frac{1}{C} \tag{31}$$

$$\frac{dV_{C,q}}{dt} = (\sum i_{WPP,i,q} - i_{DR,q} - \omega^*CV_{C,d})\frac{1}{C} \tag{32}$$

$$\frac{d\hat{P}_{WPP,i}}{dt} = \omega_f(\frac{3}{2}((V^*_{ref} + n_p(Q^*_{WPP,i} - Q_{WPP,i})\frac{V_{nom}}{P_{nom}})(i_{WPP,i,d}\cos(\delta_i) + i_{WPP,i,q}\sin(\delta_i))) - \hat{P}_{WPP,i}) \tag{33}$$

$$\frac{d\hat{Q}_{WPP,i}}{dt} = \omega_f(\frac{3}{2}((V^*_{ref} + n_p(Q^*_{WPP,i} - Q_{WPP,i})\frac{V_{nom}}{P_{nom}})(i_{WPP,i,d}\sin(\delta_i) - i_{WPP,i,q}\cos(\delta_i))) - \hat{Q}_{WPP,i}) \tag{34}$$

Eqs. (20)–(25) and (27)–(34) form a non-linear space–state system that defines the system dynamics. From the non-linear system, a parameter sensitivity analysis has been carried out to ascertain how each different grid-forming controller impacts overall system stability. In order to generalize the previous results to a wide range of operating conditions, the sensitivity analysis of all controller parameters (m_p, M_p, M_i, M_d, D_p and H) has been repeated for each one of the thirty considered operating points in Table 7.

Fig. 5 shows the sensitivity analysis to controller parameter variation, corresponding to case 14 in Table 7. The figure shows the dominant poles, especially the ones that might shift toward the unstable zone. Eigenvalues such as $\lambda_{13,14}$, $\lambda_{15,16}$ and λ_{20} are sensitive to changes in control parameters from all three control strategies, proving that the controller dynamics are not decoupled from each other. Specifically, $\lambda_{13,14}$ might become unstable with changes in m_p, M_i, D_p and H, confirming that unstable poles depend on parametric changes of several grid-forming control strategies. Therefore, global stability cannot be necessarily inferred from the stability of individual grid-forming strategies.

The sensitivity analysis in Fig. 5 has been carried out for the 30 considered cases, showing a very small sensitivity to load changes (Table 1). The worst operating point corresponds to the loading conditions of case 7 (i.e. the VSM-controlled cluster (WPP_3) produces 1 pu while the other two produce 0 pu), where the dominant eigenvalues $\lambda_{13,14}$ are closer to the imaginary axis.

Moreover, for each one of the considered cases, the system becomes unstable for controller parameter values that are very similar for all 30 cases. Table 2 shows the range of each controller parameter that makes the system unstable for the considered cases.

Since the controller parameters that make the system unstable are very similar for different operating points, it is possible to extend the study's conclusions in Fig. 5 to all considered cases, including the aforementioned worst-case scenario. The phase margins

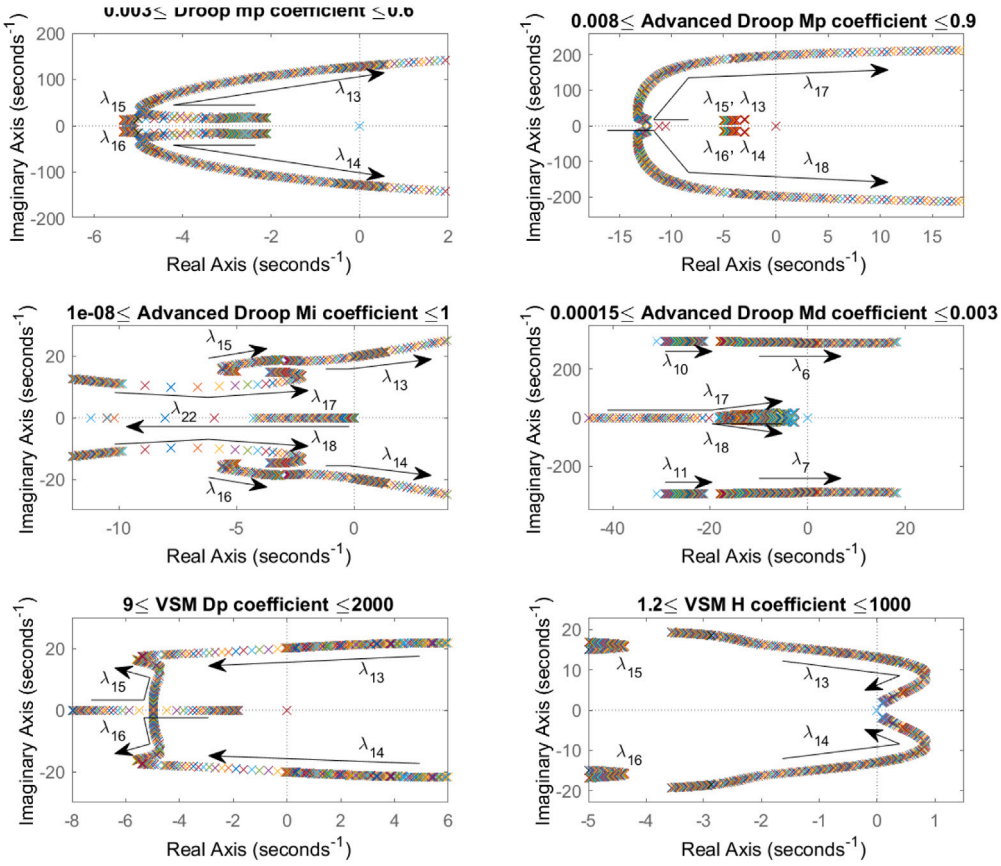

Fig. 5. Eigenvalue sensitivity for control parameter variation.

Table 2
Parameter stability limits for all considered cases.

Parameter stability limits for all considered cases						
Grid forming controller	Droop	Advanced Droop	Advanced Droop	Advanced Droop	VSM	VSM
Parameter	mp	Mp	Mi	Md	Dp	H
Stability limit range	0.41375–0.4175	0.707–0.713	0.3025–0.305	0.0017463–0.0017575	65.3–65.7	7.3–7.7

for all the considered cases are in the range of 32.34° to 33.94°, therefore showing that the controlled system is robust in terms of stability within the full range of loading conditions of the three WPP clusters.

On the other hand, the participation factors in Fig. 6 allow the analysis of each state-variable's impact on the eigenvalues. The system's eigenvalues are divided between the ones affected by the power-related states and those influenced by current and voltage states, which are not under study. Generally, the eigenvalues are simultaneously influenced by states related to all three grid-forming control strategies. Some eigenvalues, such as λ_5 and λ_{22}, depend strongly on the PI controller variables γ_n of the advanced droop controller.

These analyses allow the identification of the most influential eigenvalues to the controlled state-variables and their sensibility to the control parameters. The control parameters are then tuned to the values in Table 5 to achieve the system's desired response.

3.2. Fault ride through strategy

The system is tested for fault response by analysing a symmetrical three-phase fault. This fault is applied to the 66 kV array cable as shown in Fig. 1. The fault clearance takes about 300 ms.

Current is limited to $I_{max} = 1.2 \cdot I_n$, and an anti-windup method is required to restrict the integral action when the system reaches the saturation limits. In WTGs' P/ω control, a droop gain (m_p) is employed by (35). Nevertheless, when a fault occurs within the system, a non-linear response is observed. To address this issue, the gain is temporarily reduced to a value known as $m_{p,fault}$ immediately upon fault detection. α can take two values as defined in (36). Once the fault is cleared, this parameter gradually returns to its initial value (m_p). This methodology is proven in droop control and advanced droop control.

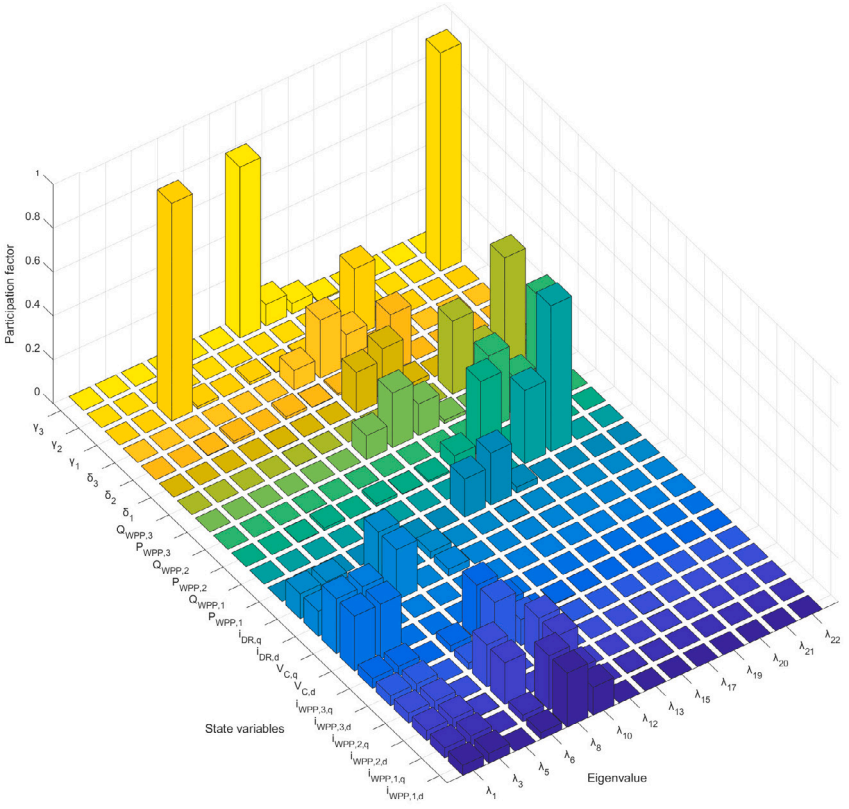

Fig. 6. Participation factor depending on state-variable and eigenvalue.

In VSM control, there is an initial value of D_p. In faults, the value transitions to $D_{p,fault}$. This adaptive control mechanism ensures system stability and reliable response during fault conditions, contributing to the overall robustness of the power grid.

$$m_p = \alpha \cdot m_{p,fault} \tag{35}$$

$$\alpha = \begin{cases} 1, & I_n \leq 1 p.u. \\ 0.2, & I_n > 1 p.u. \end{cases} \tag{36}$$

4. Results

Following the paper's aim, this section shows the results of the grid-forming controllers during active power reference variations in the described system in Section 2. The active power reference steps are applied with the same grid-forming controller in all the WPP clusters and with different grid-forming controllers in each WPP cluster to validate the grid-forming controller interoperability. Additionally, the section includes results during faults to validate the proposed fault-ride-through strategy.

4.1. Active power reference steps

The first step is validating each grid-forming controller operation when the three WPP clusters implement the same controller. Fig. 7 shows an active power step applied to the first cluster WPP_1. The active power reference P^*_{WPP1} decreases from 0.8 p.u. to 0.625 p.u. Each graph shows the active power in each WPP cluster. The results show that there is power coupling between the WPP clusters. Moreover, the advanced droop results obtain the best response with less overshooting than the droop and the VSM. The coupling between WPP clusters is also better using the advanced droop.

The following step is the interoperability evaluation of the three grid-forming power controllers. The first WPP cluster (WPP_1) implements a droop controller, the second cluster (WPP_2) employs an advanced droop controller, and the third cluster (WPP_3) implements a VSM controller.

Fig. 8 shows the interactions between the three grid-forming controllers for active power step changes. The interaction is tested by applying a power step in each different WPP cluster from their initial value (WPP_1 = 0.8 pu; WPP_2 = WPP_3 = 0.75) to a 0.625 pu. All controllers have been tuned to show the same rise time for active power and reactive power step changes.

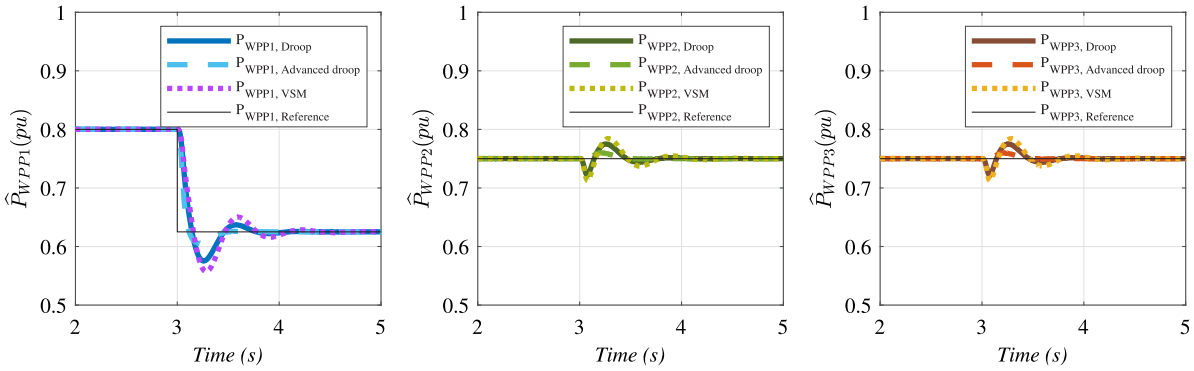

Fig. 7. Comparison of grid-forming controller performance for each WPP during active power step changes in WPP_1.

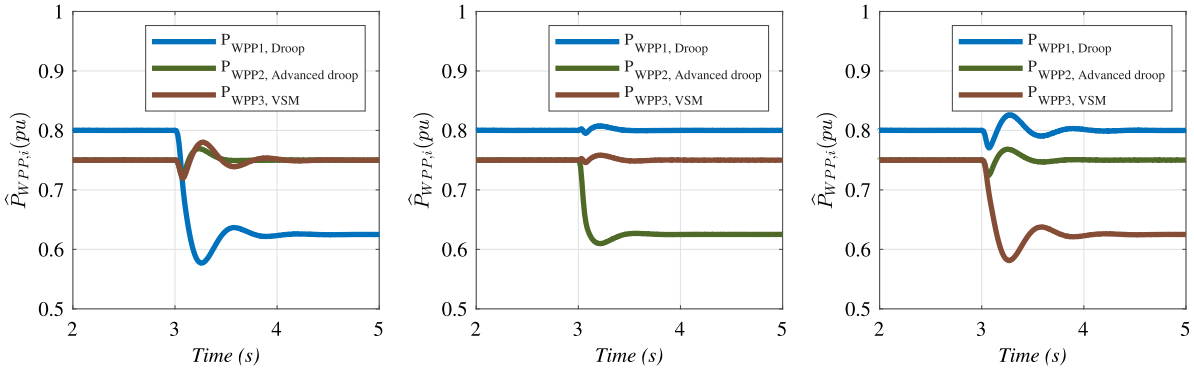

Fig. 8. Interaction between different grid-forming controllers for active power step changes in each WPP.

Clearly, the interaction is relatively large when the active power step change occurs in the WPP with the droop control (WPP_1) or with the VSM control (WPP_3). On the other hand, the interaction is much smaller when the active power set-point change occurs in the WPP with advanced droop control (WPP_2), as the additional degrees of freedom for the grid forming controller allow for a better decoupling of system dynamics and active power sharing.

In any case, the interoperability of the three grid-forming controllers is also validated in a realistic scenario of a DR-based offshore WPP.

4.2. Communication loss to the WPP controller

Secondary control is included within the WPP controller, which send active power set-points to the individual WTGs. Therefore, a study on the communication loss between cluster WPP_1 and the WPP controller is carried out. Fig. 9 shows the results when a reference step of −0.175 pu is applied to the clusters WPP_1 during the loss of communication with the WPP controller.

The communication loss occurs at 2 s. The active power reference P^*_{WPP1} decreases 0.175 pu at 3 s, and the WPP controller changes the power reference $\sum P^*_{WPPi}$, which reduces the off-shore AC voltage. There is no communication between the WPP controller and the cluster WPP_1, so the WPP control is not receiving the active power P_{WPP1}, and the cluster WPP_1 is not receiving the active power reference change P^*_{WPP1} and the voltage reference V^*_{ref} that calculates the WPP controller. The system remains stable as shown in Fig. 9, but the reactive power sharing is not optimal because each cluster is applying a different voltage reference V^*_{ref}. Nevertheless, the active power sharing works as expected. None of the clusters are receiving an active power reference change. Then, the power reference change is assumed by the three clusters and each cluster reduces the generated active power in the same ratio until the active power transmitted by the DR is controlled (0.0875 pu each one, that is a total of 0.2625 pu as the WPP controller is not detecting the active power reduction of WPP_1).

4.3. Fault-ride-through

The following step consists of validating the fault-ride-through capability of the grid-forming controllers. This includes testing the three different controllers implemented in each WPP cluster (WPP_1: droop; WPP_2: advanced droop; WPP_3: VSM). A fault is applied to the 66 kV AC offshore grid and cleared after 300 ms.

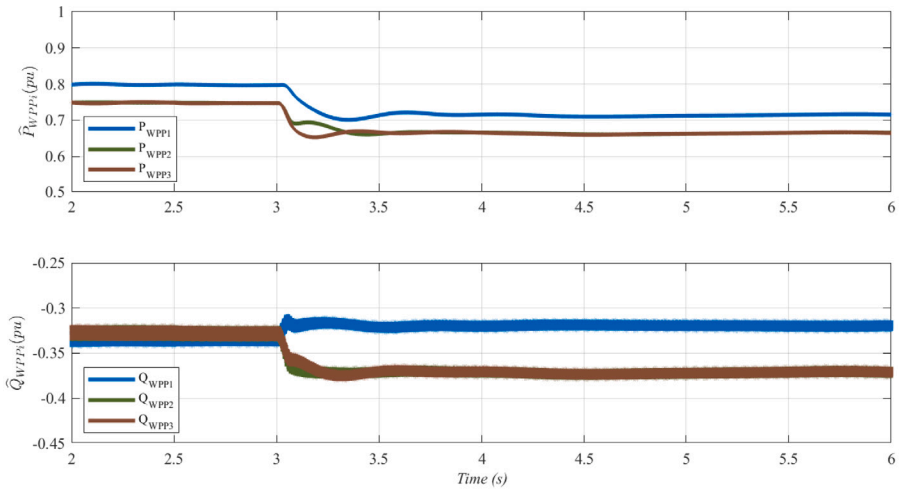

Fig. 9. Performance during an active power reference step when communication loss between the WPP controller and the cluster WPP_1.

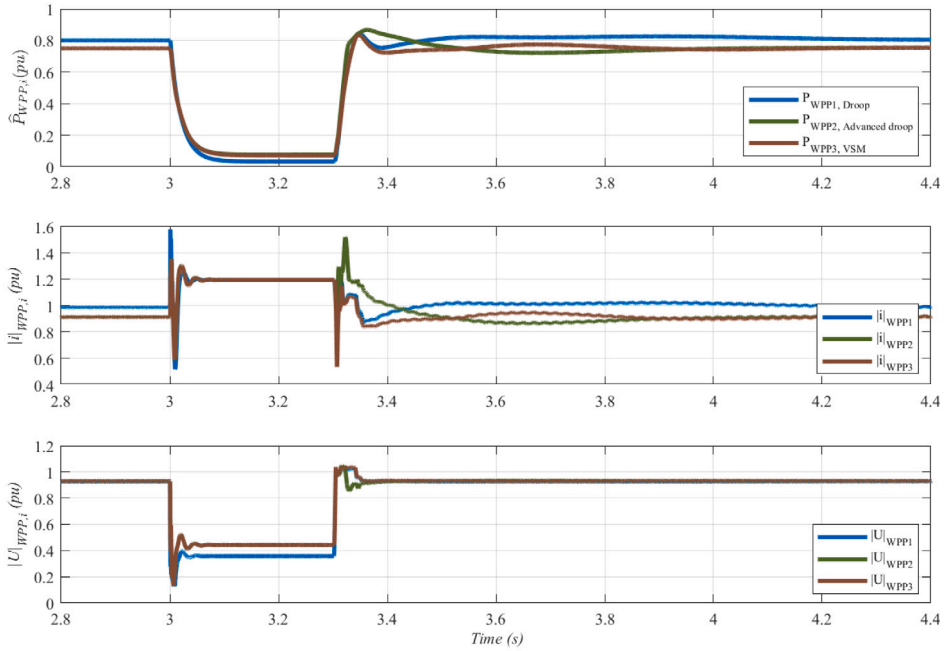

Fig. 10. Comparison of grid-forming controller performance for each WPP cluster during faults (active power, current and voltage).

Fig. 10 shows active power, current module, and voltage module drop in each WPP cluster during faults. The implemented fault-ride-through strategy achieves a fast grid recovery in less than 150 ms after fault clearance. When the fault is cleared, the system remains controlled and stable. Currents increase during the fault up to the limited value (1.2 p.u.). Simulations conclusively demonstrate compatibility when implementing all three types of control in the same system, showcasing their ability to work harmoniously together during fault.

A current limitation is implemented during a fault event to prevent potential damage to the components. Once the fault is cleared, the current is restored to its normal state. WPP1, where the fault occurs, undergoes the most significant voltage drop. Upon clearing the fault, the voltage returns to its initial state. Minimizing current limitation relative to its initial value necessitates more significant adjustments to specific parameters of the $P-\omega$ control. This is attributed to the reduced margin of operation, emphasizing the delicate balance between mitigating potential damage during faults and the subsequent need for adjustments in control parameters for optimal system performance.

5. Conclusions

This paper analyses the interoperability between three grid-forming control strategies (droop control, advanced droop control, and VSM) in a DR-connected offshore WPP. The WPP consists of three clusters of WTGs. Each grid-forming control strategy has been validated separately (the three WTG clusters implement the same controller) and with the other control strategies (each cluster implements a different grid-forming control).

The presented small signal stability analysis shows how each grid-forming control parameter affects the system stability, in addition to detecting the contribution of each control parameter to the stability of each state variable. The study shows that the most relevant dominant eigenvalues are influenced simultaneously by parameters of the three grid-forming control strategies. Therefore, the analysis of the complete system is paramount when a new grid-forming WTG cluster is to be connected. For example, it has been shown that eigenvalues $\lambda_{13,14}$ may cause instability due to control parameter changes in any of the grid-forming WPP clusters (droop M_p coefficient, advanced droop M_p and M_i coefficients and VSM H and D_p). The oscillations caused by these eigenvalues are in the range from 3.1 Hz to 16 Hz.

Additionally, the participation factors show that there is a relatively large decoupling between current and voltage loop dynamics and active and reactive power dynamics. This result shows that the design of inner and outer loops for the WPPs can be carried out independently of each other.

The sensitivity studies for 30 cases have shown that the stability margins, defined as the maximum variation of a control parameter leading to instability, are relatively independent of the operating point. The 30 cases show a 0.7% variation in the relative position of the dominant eigenvalues from their nominal value. The system's robustness was also assessed by calculating the phase margin, resulting in a range of 32.34° to 33.94° among the considered cases. The worst-case scenario corresponds to case 7, where the VSM-controlled cluster (WPP_3) produces 1 pu while the others produce 0 pu. These results confirm the analysis's validity and the system's overall robustness for any load condition.

From the large signal studies, it is clear that classical droop and VSM cause larger disturbances on the active power response of the other clusters, whereas active power step changes on the advanced droop WPP have better damping and lead to smaller active power oscillations on the other clusters. The likely reason is that the advanced droop has additional degrees of freedom that allow decoupling of active power dynamics and active power sharing.

The effect of communication loss between the WPP controller and the WTG controller has been studied, and it has been shown that secondary control is lost for both active and reactive power. Nevertheless, primary control remains stable and ensures reasonable sharing of active power amongst WTGs. During communication loss, the reactive power sharing performance is not optimal as the central controller can no longer dispatch the adequate voltage set-points and/or reactive power references to the WTGs. In any case, the system is robust against communication loss, albeit with a degraded performance.

Finally, the WTGs implement a fault-ride-through strategy to recover the system after faults that involves modifying the parameters of the grid-forming control when during faults, and once the fault is cleared, these values revert to their original state. This method has been tested through simulations with the described DR-based offshore WPP, confirming the good operation during faults and a soft restoration of the transmission power after fault clearance.

Therefore, this work has shown that wind turbine clusters with different grid forming strategies can be connected to the same DR-HVDC converter with good small and large signal dynamic behaviour for a large range of operating conditions. In any case, controller design and tuning have to be verified by using the complete system models, as all kind of grid-forming controllers largely influence the critical dominant poles of the complete system (e.g. $\lambda_{13,14}$).

CRediT authorship contribution statement

Adrián Beneit-Barajas: Writing – review & editing, Software, Methodology, Investigation, Formal analysis, Conceptualization. **Patricia Penades-Huesca:** Writing – original draft, Methodology, Investigation, Data curation, Conceptualization. **Jaime Martínez-Turégano:** Writing – review & editing, Writing – original draft, Validation, Supervision, Project administration, Methodology, Investigation, Formal analysis, Conceptualization.

Acknowledgements

Authors would like to acknowledge the support of the Spanish Research Agency through grant PID2020-112943RB-I00 funded by MCIN/AEI/10.13039/501100011033, grant PDC2021-121077-I00 funded by MCIN/AEI/10.13039/501100011033 and by the European Union NextGenerationEU/PRTR, grant PRE2021-100779 funded by MCIN/AEI/ 10.13039/501100011033 and by "ESF Investing in your future", the support of Generalitat Valenciana through grant CIAICO/2021/340, and grant INVEST/2022/439 funded by Generalitat Valenciana and the European Union Next GenerationEU/PRTR.

Appendix

Table 3 shows three of the operating point where the system has been linearized, Table 5 shows the parameters of the three grid forming controllers, Table 6 shows the electrical parameters of the overall system, and Table 4 shows the system eigenvalues for the selected operating point for the results ($P_{WPP1} = 0.8\ pu, P_{WPP2} = P_{WPP3} = 0.75\ pu$).

Table 3
System values for theoretical study.

Electrical circuit			
$R_{WPP} = 9.5220 \cdot 10^{-6}$ Ω;	$L_{WPP} = 6.8196 \cdot 10^{-7}$ H;	$C = 0.1337$ F	
$C = 3.864$ F;	$L_{DRT} = 2.526 \cdot 10^{-8}$ H;	$R_{DRT} = 2.381 \cdot 10^{-6}$ Ω	
$\omega_f = 10\ \frac{\text{rad}}{\text{s}}$;	$P_{nom} = 400$ MW;	$V_{nom} = 690$ V	
Equilibrium values for linearization 1			
$i_{WPP,1,d} = 348.7$ kA;	$i_{WPP,2,d} = 326.3$ kA;	$i_{WPP,3,d} = 326.3$ kA	
$i_{WPP,1,q} = 238.3$ kA;	$i_{WPP,2,q} = 233.1$ kA;	$i_{WPP,3,q} = 233.1$ kA	
$P_1^* = 320$ MW;	$P_2^* = 300$ MW;	$P_3^* = 300$ MW	
$P_1 = 320$ MW;	$P_2 = 300$ MW;	$P_3 = 300$ MW	
$Q_1^* = 0$ MVA;	$Q_2^* = 0$ MVA;	$Q_3^* = 0$ MVA	
$Q_1 = -161$ MVA;	$Q_2 = -161$ MVA;	$Q_3 = -161$ MVA	
$\delta_1 = 0.133$ rad;	$\delta_2 = 0.129$ rad;	$\delta_3 = 0.129$ rad	
$\gamma_1 = 0$;	$\gamma_2 = 0$;	$\gamma_3 = 0$	
$V_{C,d} = 580$ V;	$V_{C,q} = 40$ V;	$i_{DR,d} = 1049.3$ kA	
$i_{DR,q} = 0.33$ kA;	$V_{DR} = 579$ V;	$\delta_{DR} = 0$ rad	
Equilibrium values for linearization 2			
$i_{WPP,1,d} = 438.8$ kA;	$i_{WPP,2,d} = 438.6$ kA;	$i_{WPP,3,d} = 438.6$ kA	
$i_{WPP,1,q} = 233.2$ kA;	$i_{WPP,2,q} = 233.2$ kA;	$i_{WPP,3,q} = 233.2$ kA	
$P_1^* = 400$ MW;	$P_2^* = 400$ MW;	$P_3^* = 400$ MW	
$P_1 = 400$ MW;	$P_2 = 400$ MW;	$P_3 = 400$ MW	
$Q_1^* = 0$ MVA;	$Q_2^* = 0$ MVA;	$Q_3^* = 0$ MVA	
$Q_1 = -132$ MVA;	$Q_2 = -132$ MVA;	$Q_3 = -132$ MVA	
$\delta_1 = 0.171$ rad;	$\delta_2 = 0.171$ rad;	$\delta_3 = 0.171$ rad	
$\gamma_1 = 0$;	$\gamma_2 = 0$;	$\gamma_3 = 0$	
$V_{C,d} = 575$ V;	$V_{C,q} = 52$ V;	$i_{DR,d} = 1379.1$ kA	
$i_{DR,q} = 1.1$ kA;	$V_{DR} = 573$ V;	$\delta_{DR} = 0$ rad	
Equilibrium values for linearization 3			
$i_{WPP,1,d} = 42.4$ kA;	$i_{WPP,2,d} = 42.37$ kA;	$i_{WPP,3,d} = 42.36.3$ kA	
$i_{WPP,1,q} = 23.83$ kA;	$i_{WPP,2,q} = 23.83$ kA;	$i_{WPP,3,q} = 23.83$ kA	
$P_1^* = 40$ MW;	$P_2^* = 40$ MW;	$P_3^* = 40$ MW	
$P_1 = 40$ MW;	$P_2 = 40$ MW;	$P_3 = 40$ MW	
$Q_1^* = 0$ MVA;	$Q_2^* = 0$ MVA;	$Q_3^* = 0$ MVA	
$Q_1 = -202$ MVA;	$Q_2 = -202$ MVA;	$Q_3 = -202$ MVA	
$\delta_1 = 0.02$ rad;	$\delta_2 = 0.02$ rad;	$\delta_3 = 0.02$ rad	
$\gamma_1 = 0$;	$\gamma_2 = 0$;	$\gamma_3 = 0$	
$V_{C,d} = 588$ V;	$V_{C,q} = 50$ V;	$i_{DR,d} = 133.2$ kA	
$i_{DR,q} = 0.025$ kA;	$V_{DR} = 573$ V;	$\delta_{DR} = 0$ rad	

Table 4
Eigenvalues.

Eigenvalues			
$\lambda_{1,2} = -10.283 \pm 2486.4i$;	$\lambda_{3,4} = -10.385 \pm 1858.2i$;	$\lambda_5 = -997.84$;	$\lambda_{6,7} = -16.183 \pm 312.67i$
$\lambda_{8,9} = -30.882 \pm 313.82i$;	$\lambda_{10,11} = -25.482 \pm 312.28i$;	$\lambda_{12} = -56.426$;	$\lambda_{13,14} = -2.8545 \pm 18.577i$
$\lambda_{15,16} = -4.996 \pm 14.917i$;	$\lambda_{17,18} = -12.377 \pm 12.997i$;	$\lambda_{19} = -10.51$;	$\lambda_{20} = -11.21$
$\lambda_{21} = -11.211$;	$\lambda_{22} = -0.0010001$		

Table 5
System control parameters.

WT central controller				
$K_{p,Vref} = 10^{-7}$;	$K_{i,Vref} = 10^{-5}$;			
WT grid-forming power control				
Droop:	$m_p = 0.01$;	$m_i = 0$;	$m_d = 0$;	$m_{p,fault} = 0.002$
Advanced Droop:	$M_p = 0.01$;	$M_i = 0.00001$;	$M_d = 0.005$;	$M_{p,fault} = 0.002$
VSM:	$D_p = 100$;	$H = 2$;		$D_{p,fault} = 500$
Reactive power control:	$n_p = 0.01$;			
WT Voltage and current control				
$K_{p,Vd} = 8000$;	$K_{i,Vd} = 60$;	$K_{p,Vq} = 9000$;	$K_{i,Vq} = 20000$	
$K_{p,Id} = 10^{-4}$;	$K_{i,Id} = 0.1$;	$K_{p,Iq} = 10^{-4}$;	$K_{i,Iq} = 0.1$	

Table 6
Electrical system parameters.

Wind power plant				
Grid-side converter:	400 MW;	690 Vac;	50 Hz	
Grid-side filter:	$R_T = 9.5220$ μω;	$L = 68.196$ μH;	$C = 0.1337$ F	
Transformer:	400 MVA;	0.69/66 kV;	$X_W = 0.08$ pu	
Power reference:	$P^*_{WPP1} = 320$ MW;	$P^*_{WPP2} = 300$ MW;	$P^*_{WPP3} = 300$ MW	
DR platform				
Transformer:	240 MVA;	66/43/43 kV;	$R_{DR} = 0.002$ pu;	$X_{DR} = 0.08$

Table 7
List of cases for linearization.

Study Cases															
Operating point	1	2	3	4	5	6	7	8	9	10	11	12	13	14	15
$P_{WPP,1}$	100%	50%	10%	0%	100%	10%	0%	50%	10%	10%	100%	10%	0%	80	25%
$P_{WPP,2}$	100%	50%	10%	0%	50%	100%	0%	0%	50%	100%	0%	0%	10%	75	10%
$P_{WPP,3}$	100%	50%	10%	0%	0%	10%	100%	10%	50%	10%	0%	10%	0%	75	100%
Operating point	16	17	18	19	20	21	22	23	24	25	26	27	28	29	30
$P_{WPP,1}$	75%	0%	100%	0%	75%	0%	25%	0%	10%	80%	75%	75%	0%	50	25%
$P_{WPP,2}$	25%	80%	0%	25%	0%	25%	50%	0%	100%	0%	80%	75%	80%	25	0%
$P_{WPP,3}$	0%	10%	75%	25%	0%	0%	10%	50%	75%	10%	75%	80%	0%	75	10%

References

[1] F. Kamal, H.M.M. Maruf, B.H. Chowdhury, M. Manjrekar, DC voltage control for power sharing in MT-HVDC connecting offshore wind farm with onshore grid, in: 2019 SoutheastCon, IEEE, Huntsville, AL, USA, 2019, pp. 1–6, http://dx.doi.org/10.1109/SoutheastCon42311.2019.9020620.

[2] R. Blasco-Gimenez, S. Añó-Villalba, J. Rodríguez, F. Morant, S. Bernal, Uncontrolled rectifiers for HVDC connection of large off-shore wind farms, in: 2009 13th European Conference on Power Electronics and Applications, IEEE, pp. 1–8.

[3] R. Blasco-Gimenez, S. Ano-Villalba, J. Rodriguez-D'Derlee, S. Bernal-Perez, F. Morant, Diode-based HVdc link for the connection of large offshore wind farms, IEEE Trans. Energy Convers. 26 (2) (2011) 615–626, http://dx.doi.org/10.1109/TEC.2011.2114886.

[4] S. Bernal-Perez, S. Ano-Villalba, R. Blasco-Gimenez, J. Rodriguez-D'Derlee, Efficiency and fault ride-through performance of a diode-rectifier- and VSC-inverter-based HVDC link for offshore wind farms, IEEE Trans. Ind. Electron. 60 (6) (2013) 2401–2409, http://dx.doi.org/10.1109/TIE.2012.2222855.

[5] L. Yu, S. Miao, Y. Wang, J. Zhu, C. Zhao, Current-controlled offshore wind turbines connected with DRU-HVDC, in: 18th International Conference on AC and DC Power Transmission (ACDC 2022), Institution of Engineering and Technology, Online Conference, China, 2022, pp. 156–161, http://dx.doi.org/10.1049/icp.2022.1182.

[6] K. Wang, Q. Song, B. Zhao, Z. Yu, R. Zeng, Grid-forming control of offshore wind farms connected with diode-based HVdc links based on remote active power regulation, IEEE Trans. Sustain. Energy (2023) 1–13, http://dx.doi.org/10.1109/TSTE.2023.3343418.

[7] A. Jain, J.N. Sakamuri, N.A. Cutululis, Grid-forming control strategies for black start by offshore wind power plants, Wind Energy Sci. 5 (4) (2020) 1297–1313, http://dx.doi.org/10.5194/wes-5-1297-2020, Publisher: Copernicus GmbH.

[8] Y. Li, Y. Gu, T.C. Green, Revisiting grid-forming and grid-following inverters: A duality theory, IEEE Trans. Power Syst. 37 (6) (2022) 4541–4554, http://dx.doi.org/10.1109/TPWRS.2022.3151851.

[9] B.B. Johnson, T. Roberts, O. Ajala, A.D. Domínguez-García, S.V. Dhople, D. Ramasubramanian, A. Tuohy, D. Divan, B. Kroposki, A generic primary-control model for grid-forming inverters: Towards interoperable operation & control, in: HICSS, 2022, pp. 1–10.

[10] A. Tayyebi, F. Dörfler, F. Kupzog, Z. Miletic, W. Hribernik, Grid-forming converters–inevitability, control strategies and challenges in future grids application, in: CIRED 2018 Ljubljana Workshop, (0236) IEEE, pp. 1–8.

[11] A. Jain, J.N. Sakamuri, N.A. Cutululis, Grid-forming control strategies for blackstart by offshore wind farms, 2020, Copernicus Publications Göttingen, Germany, 2020, pp. 1–22, http://dx.doi.org/10.5194/wes-2020-34,

[12] A. Gonzalez-Cajigas, J. Roldan-Perez, E.J. Bueno, Design and analysis of parallel-connected grid-forming virtual synchronous machines for Island and grid-connected applications, IEEE Trans. Power Electron. 37 (2022) 5107–5121, http://dx.doi.org/10.1109/TPEL.2021.3127463.

[13] T. Thilekha, S. Filizadeh, U.D. Annakkage, C. Karawita, D. Muthumuni, Analysis of interactions among parallel grid-forming inverters, Electr. Power Syst. Res. 223 (2023) 109652, http://dx.doi.org/10.1016/J.EPSR.2023.109652.

[14] S.Z. Almutairi, Dynamic interactions between parallel grid-forming inverters in a microgrid, Appl. Sci. 13 (2023) http://dx.doi.org/10.3390/app13126989.

[15] Y. Liu, Y. Wang, X. Liu, M. Wang, Z. Xu, H. Liu, Steady-state angle stability analysis of parallel grid-forming converters in current saturation mode, IEEE Trans. Power Electron. 38 (2023) 8039–8044, http://dx.doi.org/10.1109/TPEL.2023.3267624.

[16] J. Martínez-Turégano, S. Añó-Villalba, S. Bernal-Perez, R. Peña, R. Blasco-Gimenez, Small-signal stability and fault performance of mixed grid forming and grid following offshore wind power plants connected to a HVDC-diode rectifier, IET Renew. Power Gener. 14 (12) (2020) 2166–2175, http://dx.doi.org/10.1049/iet-rpg.2019.1264.

[17] A. Bidadfar, O. Saborio-Romano, N.A. Cutululis, P.E. Sorensen, Control of offshore wind turbines connected to diode-rectifier-based HVdc systems, IEEE Trans. Sustain. Energy 12 (1) (2021) 514–523, http://dx.doi.org/10.1109/TSTE.2020.3008606.

[18] D.H. Al-Mamoori, Z.S. Hasan, A.A. Al-Obaidi, M.H. Mussa, Enhancing the control strategy of fault ride through capability for grid connected wind farm using VSC_Hvdc, 2023, 050006, http://dx.doi.org/10.1063/5.0154771.

[19] M.G. Taul, X. Wang, P. Davari, F. Blaabjerg, Current limiting control with enhanced dynamics of grid-forming converters during fault conditions, IEEE J. Emerg. Sel. Top. Power Electron. 8 (2) (2020) 1062–1073, http://dx.doi.org/10.1109/JESTPE.2019.2931477.

[20] A. Arasteh, A. Jain, O. Göksu, L. Zeni, N.A. Cutululis, Fault ride through capability of grid forming wind turbines: A comparison of control schemes, in: The 9th Renewable Power Generation Conference (RPG Dublin Online 2021), Institution of Engineering and Technology, Online Conference, 2021, pp. 37–41, http://dx.doi.org/10.1049/icp.2021.1349.

[21] Z. Yang, G. Zhao, H. Yu, Current limiting control method with adaptive virtual impedance for grid-forming STATCOM, Energy Rep. 9 (2023-04) 453–460, http://dx.doi.org/10.1016/j.egyr.2023.03.023.

[22] T. Qoria, F. Gruson, F. Colas, G. Denis, T. Prevost, X. Guillaud, Critical clearing time determination and enhancement of grid-forming converters embedding virtual impedance as current limitation algorithm, IEEE J. Emerg. Sel. Top. Power Electron. 8 (2) (2020) 1050–1061, http://dx.doi.org/10.1109/JESTPE.2019.2959085.

[23] J. Martínez-Turégano, S. Añó-Villalba, S. Bernal-Perez, R. Blasco-Gimenez, Aggregation of type-4 large wind farms based on admittance model order reduction, Energies 12 (9) (2019) 1730, http://dx.doi.org/10.3390/en12091730.

[24] J. Guerrero, L. GarciadeVicuna, J. Matas, M. Castilla, J. Miret, Output impedance design of parallel-connected UPS inverters with wireless load-sharing control, IEEE Trans. Ind. Electron. 52 (4) (2005) 1126–1135, http://dx.doi.org/10.1109/TIE.2005.851634.

[25] J.M. Guerrero, J.C. Vasquez, J. Matas, L.G. De Vicuna, M. Castilla, Hierarchical control of droop-controlled AC and DC microgrids—A general approach toward standardization, IEEE Trans. Ind. Electron. 58 (1) (2011) 158–172, http://dx.doi.org/10.1109/TIE.2010.2066534.

[26] J. Guerrero, L. GarciadeVicuna, J. Matas, M. Castilla, J. Miret, A wireless controller to enhance dynamic performance of parallel inverters in distributed generation systems, IEEE Trans. Power Electron. 19 (5) (2004) 1205–1213, http://dx.doi.org/10.1109/TPEL.2004.833451.